Diurnal wind cycles forcing inertial oscillations: A latitude-dependent resonance phenomenon

Ryosuke Shibuya[1], Kaoru Sato[1], Mikio Nakanishi[2]

[1]*Department of Earth and Planetary Science, University of Tokyo, Tokyo, Japan*

[2]*Department of Earth and Ocean Sciences, National Defense Academy, Yokosuka, Japan*

Corresponding author: Ryosuke Shibuya

University of Tokyo, 7-3-1 Hongo, Bunkyo-ku, Tokyo 113-0033, Japan

E-mail: shibuya@eps.s.u-tokyo.ac.jp.

Accepted in *J. Atmos. Sci.* on September 6, 2013

Abstract

The latitudinal dependence of inertial oscillation (IO) in a diurnally-evolving atmospheric boundary layer (ABL) is examined using a large eddy simulation (LES). Previous studies that used LES were unable to simulate such an ABL on a time scale of several days due to high computational cost. By using an LES with a simple radiation scheme, the present study has succeeded in simulating the diurnal behavior of the ABL above the nocturnal stable layer as a function of the latitude. The reality of model simulations is confirmed by comparison with Wangara experiments.

It is shown that a resonance-like amplification of the IO appears only at two latitudes where the respective inertial periods are 24 h and 12 h. A horizontal wind oscillation with strong dependence on latitude is observed during an entire day. The oscillation amplitude is maximized slightly above the nocturnal stable layer. It seems that this maximum corresponds to the nocturnal low-level jet, whose mechanism is explained in terms of IO. Thus, the IO shown in the present study includes the nocturnal jet as a structural component. It is also shown that a wave-like structure whose phases propagate downward with near-inertial frequency at each latitude is observed above the ABL at all latitudes. This feature is consistent with that of inertia-gravity waves propagating energy upward. Previous observational and model studies indicate the dominance of inertia-gravity waves with inertial frequencies in the middle and high latitudes in the lower stratosphere. Results of the present study suggest that the IO in the ABL is a possible source of such inertia-gravity waves.

[269 words]

1. Introduction

The atmospheric boundary layer (ABL) is an important atmospheric layer in which humans often interact with through various activities. Therefore, it is inevitable to understand the dynamics of the ABL in terms of temporal and spatial variations, and material exchanges with the free atmosphere. In particular, the diffusion of radioactive substances into the atmosphere has drawn strong public attention due to the nuclear accident that occurred in Fukushima, Japan, in March 2011. This paper focuses on a diurnal cycle of the ABL and its dependence on latitude.

The thermal structure of the ABL varies with a period of one day due to the rotation of the earth (Stull 1988). A mixed layer often develops during daytime due to temporally varying solar radiation, while during nighttime, when solar radiation does not reach the surface, radiative cooling dominantly occurs and a stable nocturnal boundary layer near the ground develops. The rotation of the earth also has a dynamic effect on atmospheric flow via the Coriolis force and can initiate IO (Blackadar 1957). Low-level jets are frequently observed in the nocturnal atmosphere, and generate wind shear as a source of turbulent fluxes (Mahrt et al. 1979; Smedman 1988; Banta et al. 2006). These low-level jets are characterized by a maximum wind speed around several hundred meters above the surface (Thorpe and Guymer 1977; Van Ulden and Wieringa 1996) and are considered to be caused by IO (Lundquist 2003). It should be noted that the low-level jets are not solely generated by IO. There are other mechanisms which can initiate the low-level jets such as slope effects (Holton 1967), frontal dynamics (Ostdick and Blumen 1997) and the combination of these mechanisms (Jiang et al. 2007). Baas et al. (2009) examined the climatology of the ABL at Cabauw, the Netherlands, which is a topographically flat measurement site. They used a 200 m mast equipped with propeller

vanes and cup anemometers and a 1290 MHz wind profiler to conduct their observations. According to this previous study, the peak height of low-level jet is often located near the top of a nocturnal inversion.

Initial studies (e.g. Blackadar 1957) primarily discussed IO as an undamped oscillation with an inertial frequency (f) around the equilibrium profile in the boundary layer. Blackadar (1957) introduced a conceptual nocturnal model for the nocturnal IO above the nocturnal inversion layer: During daytime, the terms of turbulent stress associated with active convection caused by solar radiation is dominant in the momentum equations of the mean field in the boundary layer. In other words, the Coriolis force, the pressure gradient force and the momentum deposition by the convective turbulence are largely balanced. Hence, the wind is not in the geostrophic balance. On the other hand, during nighttime, the turbulent motions rapidly diminish and the winds tend to be in geostrophic balance above the nocturnal inversion layer near the ground. As there is a significant departure from the geostrophic balance of the wind vector which is maintained by turbulent motions even during the transition from day to night, a free oscillation of nocturnal winds occurs around the geostrophically balanced wind vector during nighttime. Van de Wiel et al. (2010) incorporated frictional effects of the nocturnal boundary layer into Blackadar's theory. It was shown that the nocturnal wind profile oscillates around the nocturnal equilibrium wind vector rather than the geostropic wind vector. Baas et al. (2012) demonstrated the validity of the analytical model of Van de Wiel et al. (2010) by using composite hodographs, and discussed the limitations of this model around the sunset time.

Many other studies used analytical approaches to discuss the numerous physical aspects of IO (e.g., Singh et al. 1993; Tan and Farahani 1998; Shapiro and Fedorovich

2010, Schroeter et al. 2012). A number of previous studies of IO, however, have focused on the source of nocturnal low-level jets, and hence, have only focused on the lower part of the nighttime ABL (e.g., Whiteman et al. 1997; Ostdiek and Blumen 1997; Lundquist 2003). The present paper focuses on IO for all height regions of the ABL. Moreover, by taking it into account that the period of the IO is different at each latitude and that the ABL evolves diurnally, we can infer a possibility in which a resonance-like phenomenon occurs in the ABL at latitudes where the inertial frequency accords with diurnal frequency or its higher harmonics. The present study examines the interaction between IO and a diurnally-evolving ABL, and its dependence on latitude by utilizing a large-eddy simulation (LES) model.

LES is a powerful tool to study the dominant turbulent motions of the ABL (e.g., Deardorff 1974; Moeng 1984; Mason and Derbyshire 1990; Sullivan et al. 1994; Brown et al. 2002). A nocturnal IO that is accompanied by a low-level jet has been reproduced in LES models (e.g., Kosović and Curry 2000; Basu et al. 2008). However, there have been few studies that examine the IO of a diurnally-evolving ABL, since only a one-day cycle of the ABL has been simulated in LES models thus far. This is mainly due to high computational cost for the simulation by the models over multiple days, which is needed to cover a large computational domain with fine spatial resolution allowing us to capture daytime large-scale eddies and to resolve nighttime small-scale eddies. Since the purpose of this study is to elucidate the diurnal change of the whole structure of ABL over multiple days, we use a relatively coarse grid resolution which is not necessarily sufficient to resolve small eddies in the nocturnal stable boundary layer. This issue regarding the grid resolution will be carefully discussed later. On the other hand, radiative cooling is a dominant forcing factor at night (e.g., Baas et al. 2009). Thus we

incorporate a simple radiation scheme into the LES model that was originally developed by Nakanishi (2000) in order to balance the energy budget of each day.

The organization of the present paper is as follows. In Section 2, a description of a LES model is given. A comparison between the LES results and an observational case study is presented in Section 3. In Section 4, features of phenomena in an ABL that incorporates diurnal forcing are described. A mechanism of a resonance-like phenomenon is revealed and discussed in Section 5. Results are discussed in Section 6. Summary and concluding remarks are made in Section 7.

2. Model description

The basic equations of the LES model used in this study are described in detail in Nakanishi (2000). This model was used by Nakanishi (2001) and Nakanishi and Niino (2009) to simulate ABLs with various stratified conditions, which compared well with observations. Specific features of the LES model will be briefly described below.

Subgrid turbulent fluxes are calculated with the two-part model of Sullivan et al. (1994), and subgrid momentum fluxes at the ground surface are determined from the Monin-Obukhov similarity theory. In this study, the drag coefficient C_D is calculated using the similarity functions of Dyer (1974) for unstable conditions and those of Kondo (1975) for stable conditions. The similarity function of Dyer (1974) is given by

$$\phi_{m,h} = 1 + 5\zeta \tag{1}$$

and that of Kondo (1975) is given by

$$\phi_{m,h} = 1 + 6\zeta/(1 + \zeta) \tag{2}$$

where $\zeta = \mathrm{z}/\mathrm{L}$ is a parameter of the stability, z is the height and L is the Obukhov length.

The subgrid turbulent fluxes of heat and moisture at the ground surface are prescribed as a function of time t. The vertical velocity vanishes at the ground surface. The lateral boundaries are periodic and the top boundary is treated as a stress-free lid. No damping is used at the top of the model domain.

The external pressure forcing is given in the form of the geostropic wind distribution:

$$\frac{1}{f}\left(-\frac{\partial p}{\partial y},\frac{\partial p}{\partial x}\right) \equiv \left(u_g, v_g\right) \tag{3}$$

where p denotes a large-scale kinematic pressure and $\left(u_g, v_g\right)$ denotes the components of geostrophic wind. Observed geostrophic winds that are observed temporally are given at every time step, in accordance with Yamada and Mellor (1975).

A simple and idealized radiative scheme is incorporated into the LES model. It is assumed that long-wave and short-wave radiations are absorbed and/or emitted only by water vapor, whose density decreases exponentially with a scale height *H* equal to 2 km. Optical thickness τ^* is written as

$$\tau^* = \tau_0^* \exp\left(-\frac{z}{H}\right) \tag{4}$$

where $\tau_0^* = 4.0$ is used as the typical value of Earth's atmosphere.

By assuming a gray atmosphere with the two-stream approximation, the equations of upward and downward fluxes for long-wave radiation are respectively obtained as

$$F^{\uparrow}(\tau^*) = \varepsilon\pi B(T_s)\exp(\tau^* - \tau_s^*) - \int_{\tau_s^*}^{\tau^*} \exp(\tau^* - \tau')\pi B[T(\tau')]\, d\tau' \tag{5}$$

$$F^{\downarrow}(\tau^*) = \int_0^{\tau^*} \exp(\tau' - \tau^*)\pi B[T(\tau')]\, d\tau' \approx \int_{\tau_t^*}^{\tau^*} \exp(\tau' - \tau^*)\pi B[T(\tau')]\, d\tau' \tag{6}$$

where $\varepsilon = 0.92$ is used for the emissivity of the ground, $\pi B(T)$ denotes a blackbody radiative flux with temperature T, and τ_s^* denotes optical thickness at the surface. The integration is made from the ground to a height of 16 km. The net flux above 16 km is

neglected, since its influence is expected to be small. From the top of the model domain to 16 km, the temperature decreases with a lapse rate of –6.5 K km^{-1}.

In the short-wave radiation scheme, only the effect of heating is considered, since the atmosphere does not emit short-wave radiation. Following Salby (2012), the idea of the "Chapman layer" is incorporated into the short-wave radiation scheme, in which the heating rate by the short-wave radiation is determined by the amount of the absorbing substance $\left(\propto \exp\left(-\frac{z}{H}\right)\right)$ and by the rate of transmission through the absorption layer located above $\left(\propto \exp\left(-\tau_0^* e^{-\frac{z}{H}}\right)\right)$. Thus, the heating rate by short-wave absorption is given as

$$\frac{\partial T}{\partial t} = C\exp\left(-\left(\tau_0^* e^{-\frac{z}{H}} + \frac{z}{H}\right)\right) \cdot F(t) \qquad (7)$$

where C is a coefficient of the heating rate and $F(t)$ denotes a time-dependent function.

C is determined so that the amount of daily mean cooling is equivalent to the amount of daily mean heating at the model top. Cooling and heating are caused by long-wave radiation and short-wave radiation, respectively. The function $F(t)$ expresses the change in solar flux.

3. Comparison with the Wangara Experiment

In order to confirm whether the proposed LES model can simulate the realistic behavior of the ABL, we compared our model results with the Wangara field observation of Day 33 and Day 34 (Clarke et al. 1971). The Wangara observation has frequently been referred to as a typical case for an ABL with clear and dry air conditions in winter (e.g., Yamada and Mellor 1975).

1

2 3.1 Numerical conditions

3 An integration was initiated using the observational values at 09:00 local standard
4 time (LST). The initial values of U, V, W and Θ were taken from Clarke et al. (1971).
5 The time series of the vertical sensible heat flux $\langle w\theta \rangle_s$ that Hicks (1981) analyzed
6 based on the Wangara experiment are used (Fig. 1), where w is the vertical velocity
7 fluctuation, θ is the potential temperature fluctuation, the angle brackets denote an
8 spatial average, and the subscript s denotes the ground surface. On the other hand, the
9 vertical moisture (i.e., latent heat) flux $\langle wq \rangle_s$ is given as

$$\langle wq \rangle_s(t) = 10^{-4} \langle w\theta \rangle_s(t) \tag{8}$$

10 where q is the specific humidity fluctuation.

11 The function $F(t)$ in the short-wave radiation scheme is given as

$$F(t) = \begin{cases} \cos\left(\dfrac{t - 12.5}{10}\pi\right), & 7.5 \leq \mathrm{mod}(t, 24) \leq 17.5 \\ 0, & \text{otherwise} \end{cases} \tag{9}$$

12 where t is time in units of hours. The roughness length is set to 0.01 m, which in
13 accordance with Yamada and Mellor (1975). The model domain size is 4 km × 4 km
14 horizontally and 2 km vertically. The domain is divided into grids of 200 × 200 × 100
15 with a uniform grid size of 20 m in all directions. It is noted that the grid size is not very
16 sufficient to resolve small eddies in the nocturnal stable boundary layer. The time step
17 for integration is 0.5 s. The geostropic winds as a pressure force are taken from the
18 Wangara experiment (Clarke et al. 1971) (Fig. 2).

19

20 3.2 Results

21 Time-height cross sections of observed and simulated potential temperature are

shown in Fig. 3, where the simulated results are averaged over each horizontal plane. Vertical profiles of observed and simulated potential temperature at different hours are shown in Fig. 4. It can be seen in the observations (Fig. 3a) that a convective mixed layer develops and is capped by a stable inversion layer during the daytime, while a strong stable layer adjacent to the surface is formed during the nighttime. These features are well simulated by our LES model (Fig. 3b). The amplitude of diurnal change in temperature in the mixed layer and the depth of the nocturnal stable boundary layer are also consistent with the observations even in this relatively coarse resolution model. This suggests that our model, which utilizes a simple radiation scheme, successfully simulated the diurnal thermal evolution of the ABL, although there are a few discrepancies that exist between the observation and simulation. At night, an increase in the potential temperature between 500 m and 1500 m in the observation was not simulated in the model. During the daytime on Day 34, the potential temperature in the simulated mixed layer was underestimated by 2-3 K. It is likely that these discrepancies are partly attributed to the lack of large-scale subsidence of air at night with high potential temperature, and partly to a slightly smaller surface heat flux for Day 34 than that of Yamada and Mellor (1975).

The observed and simulated zonal and meridional wind components are shown in Fig. 5. The simulated wind components were also horizontally averaged. It is seen that the model is able to properly reproduce the realistic properties of the daily phenomena that occur in the ABL. During daytime, the observed winds are almost vertically uniform in the convective mixed layer. The nocturnal low-level jet develops during the night. The uniform daytime winds are due to turbulent mixing, while the nocturnal jet is likely due to an IO. The evolution of these winds that were observed during the day and

night are well simulated in our model. For Day 34, the simulated meridional winds are apparently different from the observed winds. However, it should be noted that the time tendency of the simulated meridional wind for Day 34, is opposite to that of the observed meridional geostrophic wind (in Fig.2b), which is consistent with that of the observation.

4. Diurnal cycle of the ABL

To examine the dynamical interplay between inertial oscillation and the diurnal boundary layer cycle, we attempted to simulate the diurnal change of the ABL over 4 model days by using the modified LES that incorporates the simple radiation scheme.

4.1 Numerical conditions

The sensible and latent heat fluxes are respectively prescribed as

$$\langle w\theta \rangle_s(t) = \begin{cases} -0.109 \cos\left(\dfrac{t-13}{12}\pi\right), 7.0 \le t \le 19.0 \\ -0.02712 \cos\left(\dfrac{t-13}{12}\pi\right), \text{otherwise} \end{cases} \tag{10}$$

$$\langle wq \rangle_s(t) = 10^{-4} \langle w\theta \rangle_s(t) \tag{11}$$

where the coefficients are chosen to ensure a balance between the heating and cooling rates throughout the day. For simplicity, the period of daytime is set to exactly 12 hours. The sensible heat fluxes are given in the form of a sinusoidal function. However, it was confirmed that the essential features of the simulated ABL are independent of the functional form of the surface heat fluxes.

A total of 21 experiments with different latitudes were performed. The model domain was 10 km × 10 km horizontally and 2 km vertically, and was equally divided

with a uniform grid size of 40 m in all directions. As we have already mentioned, the grid size of 40 m may be coarse to resolve the nocturnal stable boundary layer. However, it should be noted that this resolution problem hardly affects our results, since the detailed structure of the nocturnal layer below a height of approximately 100 m does not play an essential role in the resonance-like mechanism which is the main topic of the present study. Time integration for each experiment was done for a 4-day period and with a time step of 2 s.

The geostrophic winds are uniformly given as $(U_g, V_g) = (3.0, 0.0)$ for all experiments. The initial conditions for horizontal wind are set to (U_g, V_g), and for the first step, vertical wind is zero. At 09:00 LST, the vertical profile of potential temperature obtained in the Wangara experiment (Clarke et al. 1971) is used as the horizontal uniform initial potential temperature field.

4.2 Results

Figure 7 shows a time-height cross section of simulated potential temperature at a latitude of 50°S. The ABL evolves periodically, and a systematic trend in potential temperature is rarely seen over the 4-day period. The top of the nocturnal stable boundary layer is located at approximately 100 m AGL.

Figure 8 shows the time-height cross sections for zonal wind at 30°S, 50°S, 14.47°S and 90°S. The diurnal evolutions of zonal wind strongly depend on latitude. The oscillation of zonal wind at 30°S is clearly defined and amplifies with time, while it is obscure for 50°S. For 14.47°S, the zonal wind is amplified every two days. For 90°S, the oscillation of zonal wind is clearly defined, even though the amplitude of oscillation is smaller than that for 30°S.

It should be noted that, regardless of latitude, maximum zonal wind oscillation is observed near 100 m AGL, which is located slightly above the nocturnal stable layer. It is also worth noting that the characteristics of a wave-like structure with phases propagating downward are seen above the ABL in Fig. 8. This structure is likely due to gravity waves propagating energy upward. The linear theory of inertial gravity waves indicates that the downward phase propagation means upward energy propagation. Thus, the wave-like structures seen in Figure 8 are consistent with the inertial gravity waves propagating energy upward. It is also seen that the amplitude maximum of the waves propagates upward during 24-48h in Fig. 8, which supports this inference. Further discussion of this structure is provided in Section 6.

Hodographs of the horizontal wind vectors, which are averaged for the mixed layer between 200 m and 800 m, are shown in Fig. 9. Regardless of latitude, the plots of each hodograph rotate counterclockwise. Note that all experiments utilize negative f, since the locations are in the Southern Hemisphere. The hodograph for 30°S is nearly circular and amplifies with time, regardless of day or night. However, for 50°S, the daytime hodograph is largely disturbed, while the nighttime hodograph is circular and rotates around the geostrophic wind $(3.0\mathrm{m\ s^{-1}}, 0.0\mathrm{m\ s^{-1}})$. The hodographs for 14.47°S and 90°S also have interesting characteristics. For 90°S, the hodograph is circular during the day and night, although the daytime plot is slightly distorted. For 14.47°S, the oscillation is amplified every two days, as seen in Fig. 8. An interesting feature is that the meridional wind component is always southward during the entire 4-day period.

To quantify the latitudinal dependence of the oscillations, the amplitude is defined as

$$A = \overline{\sqrt{\left(u - u_g\right)^2 + \left(v - v_g\right)^2}} \tag{12}$$

where the equilibrium value for this oscillation corresponds to the geostrophic wind $(u_g, v_g) = (3.0\text{m s}^{-1}, 0.0\text{m s}^{-1})$ that is balanced with the pressure field given in this model, and the overbar denotes a time average. Figure 10 shows the amplitude of IO averaged over the third and fourth days as a function of latitude. The inertial period of each latitude is also shown. It is clear at what latitudes that amplitude is maximized. The largest peak is located at 30°S, whose inertial period is 24 h, and two small peaks are observed around 14.47°S and 90°S, whose inertial periods are 48h and 12 h, respectively.

These results suggest that the latitudinal variation of amplitude, as provided by the LES, proves the presence of some type of resonance. The Q value, which expresses the degree of resonance, is estimated as

$$Q = \frac{\omega_0}{\omega_1 - \omega_2} \approx 2.43 \tag{13}$$

where ω_0 is the frequency of the peak amplitude, and ω_1 and ω_2 are two frequencies with a half of the peak amplitude, respectively. The mechanisms of the IO and its dependence on latitude will be discussed in the next section.

5. Mechanisms of resonance

The one-dimensional horizontal momentum equations for the ABL can be expressed as

$$\frac{\partial u}{\partial t} - fv = \frac{\partial \tau_x}{\partial z}, \tag{14}$$

and

$$\frac{\partial v}{\partial t} + f(u - u_g) = \frac{\partial \tau_y}{\partial z}, \tag{15}$$

where τ_x and τ_y denote the horizontal turbulent subgrid stress tensor in the x and y

directions, respectively. From (14) and (15), the following equation in the form of a forced oscillation is derived:

$$\frac{\partial^2 u}{\partial t^2} + f^2(u - u_g) = \frac{\partial}{\partial z}\left(\frac{\partial \tau_x}{\partial t} + f\tau_y\right). \quad (16)$$

Equation (16) describes the oscillations with a frequency f forced by the terms on the right-hand side. This equation shows that the atmospheric motions potentially have an eigen frequency that accords with the inertial frequency. On the other hand, the forcing terms originate from the turbulent subgrid stress tensor, which varies diurnally in correspondence to the evolution of the ABL. This indicates that resonance may occur at latitudes where the inertial frequency accords with the diurnal frequency and its higher harmonics. The existence of the simulated amplitude peaks at 30°S and 90°S in Fig. 10, where the inertial periods are 24 h and 12 h, respectively, is consistent with this mechanism.

The amplification of the oscillations can also be understood by evaluating the plots on each hodograph. It is seen that by ignoring the tendency terms (i.e., $\partial/\partial t = 0$) in (14) and (15), that the equilibrium horizontal wind vector $(u_{\mathrm{eq}}, v_{\mathrm{eq}})$ should satisfy

$$v_{\mathrm{eq}} = -\frac{1}{f}\frac{\partial \tau_x}{\partial z} \quad (17)$$

and

$$u_{\mathrm{eq}} - u_{\mathrm{g}} = \frac{1}{f}\frac{\partial \tau_y}{\partial z} \quad (18)$$

As Van de Wiel et al. (2010) discussed, it can be shown that each hodograph (u, v) rotates around the equilibrium horizontal wind vector $(u_{\mathrm{eq}}, v_{\mathrm{eq}})$ by combining (14) and (15) and by assuming that the time tendencies of the equilibrium wind vector $(u_{\mathrm{eq}}, v_{\mathrm{eq}})$ are negligible:

$$\frac{\partial(u - u_{\mathrm{eq}})}{\partial t} = f(v - v_{\mathrm{eq}}) \quad (19)$$

and

$$\frac{\partial(v - v_{\mathrm{eq}})}{\partial t} = -f(u - u_{\mathrm{eq}}) \tag{20}$$

For simplicity, we assume that only two different equilibrium vectors $(u_{\mathrm{eq}}, v_{\mathrm{eq}})$ exist in one day (i.e., one for nighttime and the other for daytime), although $(u_{\mathrm{eq}}, v_{\mathrm{eq}})$ actually continuously varies. During nighttime, the equilibrium wind vector $(u_{\mathrm{eq}}, v_{\mathrm{eq}})$ is typically located near $(u_{\mathrm{g}}, v_{\mathrm{g}})$, since the turbulent stress term in (17) and (18) is almost zero above the nocturnal stable boundary layer. The equilibrium wind vector $(u_{\mathrm{eq}}, v_{\mathrm{eq}})$ for daytime would significantly differ from $(u_{\mathrm{eq}}, v_{\mathrm{eq}})$ for nighttime, since the turbulent terms become large. Thus, (19) and (20) imply that the wind vector rotates around the equilibrium wind vector, which is different for daytime and nighttime scenarios.

The following assumption clearly explains the amplifications of the oscillation simulated for 30°S. It appears that the wind vectors rotate around their respective equilibrium wind vectors $(u_{\mathrm{eq}}, v_{\mathrm{eq}})$ during the nighttime (N) and daytime (D) for 30°S, as shown in Fig. 11. In this figure, the equilibrium wind vectors were determined by fitting a part of each hodograph to a circular arc and estimated at the center of the circular arc. In fact the equilibrium wind vectors estimated in this way accord with the vectors determined theoretically by (17) and (18) using simulation data that are averaged over the daytime and the nighttime, respectively. In order to understand the relationship between the amplification of the oscillation and the above equilibrium wind vectors, schematic diagrams of the hodographs are shown in Fig. 12. For the hodograph for 30°S, where the inertial period is 24 h, the wind vector rotates 180 degrees in half a day. The radius of the rotation around $(u_{\mathrm{eq}}, v_{\mathrm{eq}})$ becomes larger every half of a day at timing of morning/evening transition. This feature is attributable to the different

positions of the daytime/nighttime equilibrium vectors plotted on the hodograph. It is also important that the amplification is not dependent on the initial value of a wind vector (i.e., the position of a wind vector at 06:00 LST on the hodographs). At other latitudes, the hodographs are complex and unsynchronized, and do not show an amplification, since the angle by which the wind vector rotates around $(u_{\mathrm{eq}}, v_{\mathrm{eq}})$ in half a day is not 180 or 360 degrees. This is likely the mechanism that amplifies the IO at 30°S.

For 90°S, however, the amplification of the IO cannot be explained by the above mechanism. Figure 12b indicates that the wind vector continuously traces the same circle, since the wind vector rotates 360 degrees in half a day, which causes its position on the hodograph to remain unchanged at morning/evening transition. To understand such a mechanism for 90°S, it is necessary to consider that there are two different equilibrium wind vectors that exist during the day (i.e., in the morning and afternoon). As shown in Fig. 11, there are different equilibrium vectors for the morning and afternoon for 90°S. This difference is attributed to the characteristics of the development of the convective layer. As seen in Fig. 8, strong wind shear is located at the top of the convective layer during the development of the ABL in the morning. Thus, the vertical gradient of turbulent stress is large in (17) and (18), and hence, a deviation from $(u_{\mathrm{eq}}, v_{\mathrm{eq}})$ occurs. In the afternoon, $(u_{\mathrm{eq}}, v_{\mathrm{eq}})$ changes due to the winds in the convective layer becoming well homogenized and well mixed, and hence, the vertical gradient of turbulent stress in (17) and (18) is smaller. Figure 12 shows that similarly to that for 30^{o} S, the oscillation for 90°S amplifies due to the existence of two different values of $(u_{\mathrm{eq}}, v_{\mathrm{eq}})$ for the daytime equilibrium wind vectors. However, since the amplification for 90°S is only attributed to the difference in $(u_{\mathrm{eq}}, v_{\mathrm{eq}})$ during the day,

the efficiency of the amplification is smaller than that for 30°S. It should be noted that, although such a difference in $(u_{\mathrm{eq}}, v_{\mathrm{eq}})$ is also observed at 30°S, this difference is not essential for an amplification at 30°S since this difference is smaller than the difference between daytime and nighttime.

In Fig. 10, there is a weak peak of oscillation amplitude for the lower latitudes around 14.47°S. However, the existence of this peak may not be attributed to the resonance-like phenomenon, since the peak is broad compared to that of 30°S and 90°S, and the amplitude of the oscillation does not significantly amplify with time. The departure of the equilibrium wind vector $(u_{\mathrm{eq}}, v_{\mathrm{eq}})$ from the geostrophic wind $(u_{\mathrm{g}}, v_{\mathrm{g}})$, which primarily determines the oscillation amplitude, is larger for a given turbulent forcing at lower latitudes that have a smaller Coriolis parameter f (see (17) and (18)). This indicates that the center of rotation $(u_{\mathrm{eq}}, v_{\mathrm{eq}})$ is more distant from the geostrophic wind vector $(3.0\mathrm{m\ s^{-1}}, 0.0\mathrm{m\ s^{-1}})$, and that the wind vectors illustrate a larger circle around the equilibrium wind vector $(u_{\mathrm{eq}}, v_{\mathrm{eq}})$. Thus, it is suggested that an amplitude of oscillation of $\overline{\sqrt{(u-3.0)^2+v^2}}$ increases as latitude decreases. It should be noted that the strength of turbulent forcing can be assumed to be independent of latitude in the present discussion, since the sensible/latent heat fluxes are similarly prescribed for all experiments.

Another interesting characteristic of this oscillation is its dependence on geostrophic wind (i.e., pressure gradient force). For stronger geostrophic winds, the turbulent drag force, and hence the deviation of the equilibrium wind from $(u_{\mathrm{g}}, v_{\mathrm{g}})$, should be also larger (see (17) and (18)). Thus, the departure of $(u_{\mathrm{eq}}, v_{\mathrm{eq}})$ from $(u_{\mathrm{g}}, v_{\mathrm{g}})$ becomes larger, which results in a larger illustrated circle around the equilibrium wind vector $(u_{\mathrm{eq}}, v_{\mathrm{eq}})$. This indicates that an amplitude of oscillation of

$\overline{\sqrt{(u-u_g)^2+(v-v_g)^2}}$ is larger for stronger geostrophic winds. To confirm this, additional experiments were conducted with geostrophic wind (u_g, v_g) set to $(1.5\ \mathrm{m\ s^{-1}},\ 0\ \mathrm{m\ s^{-1}})$ and $(4.5\ \mathrm{m\ s^{-1}},\ 0\ \mathrm{m\ s^{-1}})$ accordingly. Figure 13 shows the amplitudes as functions of geostrophic wind at 30°S and 50°S. Amplitude increases almost linearly as geostrophic wind speed increases for 30°S and 50°S. This result also supports the resonance mechanism discussed in this study.

6. Discussion

Oscillation amplitude was found to have a strong dependence on latitude, which is regarded as a resonance. This latitudinal dependence was found to occur during the night and day. It is important to note that the maximum oscillation amplitude of wind was located slightly above the nocturnal stable layer, which is consistent with a characteristic of IO as the mechanism of the nocturnal jet treated in previous studies. Figure 14 shows vertical profiles of zonal wind during the nighttime at 30°S. Maximum wind speeds are located around a height of 80 m (i.e., top of the nocturnal stable layer). It is considered that this location of maximum wind speed corresponds to the nocturnal jet. Thus, the IO discussed in the previous studies can be regarded as a part of the oscillation discussed in this study.

Next, to examine the wave-like structure that was observed above the convective layer in Fig. 8, horizontally-averaged frequency power spectra of the zonal wind fluctuations were obtained for 30°S, 50°S, 90°S and 14.47°S (Fig. 15). In the mixed layer that had a top around 1100 m, the power spectra have several dominant peaks for inertial frequency and diurnal frequency and its higher harmonics. In contrast, the power spectra have only one peak for inertial frequency in a free atmosphere. This implies that

the wave-like structure with an inertial frequency in the free atmosphere was excited by the forcing in the mixed layer. Using observational data, Sato et al. (1997), Nastrom and Eaton (2006), and Sato and Yoshiki (2008) reported the existence of peaks near the inertial frequency of each latitude for the frequency power spectra of observed horizontal wind fluctuations in the lower stratosphere. Sato et al. (1999) used a gravity-wave resolving general circulation model and showed that spectral peaks, which compared well with observations, are globally present near the inertial frequency in the lower stratosphere. It was also shown that these peaks are likely due to inertia-gravity waves. The waves with an inertial frequency in the free atmosphere that were simulated in the present study are possible sources of such peaks in the power spectra of the lower stratosphere.

It should be noted that the experiments in the present study were performed with idealized model settings. The period of daytime was fixed to 12 h for all experiments, even though the number of daylight hours has seasonal and latitudinal variations in the real atmosphere. However, even if the daytime length is not exactly 12 h, the dominant frequency of turbulent forcing is one day, and hence the results in this study are considered to be robust except for polar night regions.

The grid size of the LES model (40 m) may be too coarse to resolve the nocturnal stable layer explicitly. However, it should be noted that this had little effect on our results since the detailed structure of the nocturnal layer below approximately 100 m does not play an essential role in the resonance mechanism shown by this study.

7. Summary and Concluding Remarks

By introducing a simplified radiative scheme into the LES model developed by

Nakanishi (2000), the diurnal change of the ABL was examined. The evolution of the ABL, which was comparable to the observation in the Wangara experiment (Clarke et al., 1971), was successfully simulated. Using the LES, we also succeeded in simulating the periodic evolution of the ABL over a 4-day period without any systematic trends of potential temperature. Our main results are as follows.

1) A resonance-like amplification of the IO was observed under the diurnal forcing by the turbulent stress at latitudes where inertial frequency accords with diurnal frequency and its higher harmonics. This oscillation amplification can be interpreted as a resonance between the Coriolis force and turbulent stress.
2) This oscillation was present for the entire day and from the ground to the top of the daytime convective mixed layer.
3) The maximum wind speeds were located slightly above the nocturnal stable layer in the oscillation simulated in this study, which is similar to the low-level nocturnal jet (but somewhat amplified).
4) Wave structures with an inertial frequency were observed in the free atmosphere above the ABL. A downward phase propagation was consistent with the inertia-gravity waves that propagated energy upward.

We schematically illustrated the resonance mechanism of IO in terms of changes in the equilibrium wind vector.

In our experiments, an external forcing was given by a constant pressure gradient force. This is not always the case in the real atmosphere. However, such a resonance-like oscillation may be observed during calm conditions. For future studies, it will be interesting to investigate the diurnal variations of the ABL by using wind profiler network data in a systematic way like Baas et al. (2012). Moreover, such

oscillations in the ABL can be a strong source of inertia-gravity waves, which are frequently observed in the free atmosphere. Further studies from this point of view are also necessary.

Acknowledgment

The authors thank Professor Hiroaki Miura for instructive advice. This study is partly supported by the GRENE Arctic Climate Change Research Project.

Reference

Baas, P., F. C. Bosveld, H. Klein Baltink, and A. A. M. Holtslag, 2009: A climatology of nocturnal low-level jets at Cabauw. *J. Appl. Meteor. Climatol.*, **48,** 1627-1642.

Baas, P., B. J. H. Van de Wiel, L. Van den Brink, and A. A. M. Holtslag, 2012: Composite hodographs and inertial oscillations in the nocturnal boundary layer. *Quart. J. Roy. Meteor. Soc.*, **138**, 528-535.

Banta, R. M., Y. L. Pichugina, and W. A. Brewer, 2006: Turbulent velocity-variance profiles in the stable boundary layer generated by a nocturnal low-level jet. *J. Atmos. Sci.*, **63,** 2700-2719.

Basu, S., and Vinuesa J-F., and Swift A, 2008: Dynamic LES modeling of a diurnal cycle. *J Appl. Meteor. Clim.*, 47, 1156-1174

Blackadar, A. K., 1957: Boundary layer wind maxima and their significance for the growth of nocturnal inversions. *Bull. Amer. Meteor. Soc*., 38, 283-290

Brown, A. R., and Coauthors, 2002: Large-eddy simulation of the diurnal cycle of shallow cumulus convection over land. *Quart. J. Roy. Meteor. Soc.*, **120,** 1485-1512.

1 Clarke, R. H., A. J. Dyer, R. R. Brook, D. G. Reid, and A. J. Troup, 1971: The Wangara
2 experiment: Boundary layer data. Tech. Paper No. 19, Division of Meteorological
3 Physics, CSIRO, Australia, 358 pp.
4 Deardorff, J. W., 1974: Three-dimensional numerical study of the height and mean
5 structure of a heated planetary boundary layer. *Bound.-Layer meteor.,* **7,** 81-106.
6 Dyer, A. J., 1974: A review of flux-profile relationships, *Bound, Layer Meteor.*, **7,**
7 363-372.
8 Hicks, B. B., 1981: An analysis of Wangara micrometeorology: Surface stress, sensible
9 heat, evaporation, and dewfall. NOAA Tech. Memo. ERL ARL-104, NOAA/Air
10 Resources Laboratories, Silver Spring, MD, 36pp.
11 Holton, J. R. 1967: The diurnal boundary layer at low latitudes. I: The nocturnal jet.
12 *Boundary-Layer Meteorol.,* **32**, 307-327.
13 Jiang, X. N., N-C. Lau, I. N. Held, and J. J. Ploshay, 2007: Mechanisms of the Great
14 Plains low-level jet as simulated in an AGCM. *J. Atmos. Sci.,* **64**, 532-547.
15 Kondo, J., 1975: Air-sea bulk transfer coefficients in diabatic conditions. *Bound, Layer*
16 *Meteor.*, **9,** 91-112.
17 Kosović, B., and J. A. Curry, 2000: A large eddy simulation study of a quasi-steady,
18 stably stratified atmospheric boundary layer. *J. Atmos. Sci.*, **57**, 1052-1068.
19 Lundquist, J. K., 2003: Intermittent and elliptical inertial oscillations in the atmospheric
20 boundary layer, *J. Atmos. Sci.*, **60,** 2661-2673.
21 Mahrt, L., R. C. Heald, D. H. Lenschow, B. B. Stankov, and I. Troen, 1979: An
22 observational study of the structure of the nocturnal boundary layer.
23 *Bound.-Layer Meteor.,* **17**, 247-264.
24 Mason, P. J., and S. H. Derbyshire, 1990: Large-eddy simulation of the stably-stratified

atmospheric boundary layer. *Bound.-Layer Meteor.*, **53,** 177-162.

Moneg, C.-H., 1984: A large-eddy-simulation model for the study of planetary boundary-layer flows. *J. Atmos. Sci.*, **51,** 999-1022

Nakanishi, M., 2000: Large-Eddy Simulation of Radiation Fog, *Boundary-Layer Meteor.* **94,** 461-493.

Nakanishi, M., 2001: Improvement of the Mellor-Yamada turbulence closure model based on large-eddy simulation data. *Boundary-Layer Meteor.*, **99**, 349-378.

Nakanishi, M. and H. Niino, 2009: Development of an improved turbulence closure model for the atmospheric boundary layer. *J. Meteor. Soc. Japan,* **87,** 895-912

Nastrom, G. D., and F. D. Eaton, 2006: Quasi-monochromatic inertia–gravity waves in the lower stratosphere from MST radar observations. *J. Geophys. Res.*, **111,** D19103, doi:10.1029/2006JD007335.

Ostdiek, V., and W. Blumen, 1997: A dynamic trio: Inertial oscillation, deformation frontogenesis, and the Ekman-Taylor boundary layer. *J. Atmos. Sci.*, **54,** 1490-1502.

Salby, M., 2012: Physics of the Atmosphere and Climate, Cambridge University Press, Cambridge, 718pp.

Sato, K., D. J. O'Sullivan, and T. J. Dunkerton, 1997: Low-frequency inertia-gravity waves in the stratosphere revealed by three-week continuous observation with the MU radar. *Geophys. Res. Lett.*, **24**, 1739-1742.

Sato, K., Kumakura, T., Takahashi, M., 1999: Gravity Waves Appearing in a High-Resolution GCM Simulation. *J. Atmos. Sci.*, **56**, 1005–1018.

Sato, K., and Yoshiki, M., 2008: Gravity wave generation around the polar vortex in the stratosphere revealed by 3-hourly radiosonde observations at Syowa Station. *J.*

Atmos. Sci., **65**, 3719-3735.

Schroeter, J., A. F. Moene, A. A. M. Holtslag, 2012: Convective boundary layer dynamics and inertial oscillations: the influence of surface stress. *Quart. J. Roy. Meteor. Soc.*, DOI: 10.1002/qj.2069.

Shapiro, A., and E. Fedorovich, 2010: Analytical description of a nocturnal low-level jet. *Quart. J. Roy. Meteor. Soc.,* **136,** 1255-1262.

Singh, M. P., R. T. McNider, and J. T. Lin, 1993: An analytical study of diurnal wind-structure variations in the boundary layer and the low-level nocturnal jet. *Bound.-Layer Meteor.,* **63,** 397-423.

Smedman, A. S., 1988: Observations of a multi-level turbulence structure in a very stable atmospheric boundary layer. *Bound.-Layer Meteor.,* **44,** 231–253.

Sullivan, P. P., J. C. McWilliams, and C.-H. Moneg, 1994: A Subgrid-Scale Model for Large-Eddy Simulation of Planetary Boundary-Layer Flows, *Boundary-Layer Meteor.,* **71,** 247-276.

Tan, Z.-M., and M. M. Farahani, 1998: An analytical study of the diurnal variations of wind in a semi-geostrophic Ekman boundary layer model. *Bound.-Layer Meteor.*, **86,** 313-332.

Thorpe, A. J., and T. H. Guymer, 1977: The nocturnal jet. Quart. J. Roy. Meteor. Soc., **103,** 633-653.

Van de Wiel B. J. H., A. F. Moene, G. J. Steeneveld, P. Baas, F. C. Bosveld, and A. A. M. Holtslag, 2010: A conceptual view on inertial oscillations and nocturnal low-level jets. *J Atmos Sci.*, **67,** 2679-2689.doi:10.1175/2010JAS3289.1

Van Ulden, A. P., and J. Wieringa, 1996: Atmospheric boundary layer research at Cabauw. *Bound.-Layer Meteor.,* **78**, 39-69.

Whiteman, D. C., X. Bian, and S. Zhong, 1997: Low-level jet climatology from enhanced rawinsonde observations at a site in the Southern Great Plains. *J. Appl. Meteor.*, **36,** 1363-1376.

Figure Captions

Fig. 1: Time series of surface sensible flux (Km s^{-1}) as provided by the model. The dots represent estimates from the observational results (Hicks 1981).

Fig. 2: Time-height cross sections of the observed (left) zonal (U_g) and (right) meridional (V_g) components of geostrophic wind (m s^{-1}) (Yamada and Mellor 1975).

Fig. 3: Time-height cross sections of the (left) observed and (right) simulated horizontally-averaged potential temperature (°C).

Fig. 4: Vertical profiles of (left) observed and (right) simulated daytime (top) and nighttime (bottom) mean potential temperature.

Fig. 5: Time-height cross sections of horizontally-averaged (left) observed and (right) simulated (top) zonal and (bottom) meridional wind speed (m s^{-1}).

Fig. 6: Time series of surface sensible flux (Km s^{-1}) as provided by the model in the diurnal cycle simulation.

Fig. 7: Time-height cross section of horizontally-averaged simulated potential temperature (K) at 50°S.

Fig. 8: Time-height cross sections of horizontally-averaged simulated zonal wind speed (m s^{-1}) at (left, bottom) 30°S, (right, bottom) 50°S, (left, top) 14.47°S and (right, top) 90°S. The dashed lines indicate the maximum heights of the nocturnal stable boundary layer for respective latitudes.

Fig. 9: Simulated hodographs of zonal (u) and meridional winds (v) at 30°S (bottom left), 50°S (bottom right), 90°S (top left), and 14.47°S (top right). Each mark denotes the values of (u, v) at time intervals of one hour. The thick marks denote nighttime (19:00 LST – 07:00 LST) and the thin marks denote daytime (07:00 LST – 19:00 LST) values. The red, yellow, green and blue colors represent data for the first, second, third, and fourth days from the initiation of integration, respectively.

Fig. 10: Oscillation amplitude as a function of latitude. Inertial frequency (bottom), latitude (middle) and an inertial period (top) are shown. The red and blue lines represent the amplitude on the third and fourth model days, respectively. The black thick line represents the average amplitude for the third and fourth days.

Fig. 11: Simulated hodographs of the zonal (u) and meridional winds (v) at 30°S (left) and 90°S (right). The same marks in Fig. 10 are used. The numerals in the figures denote local time. N, D, AM, and PM denote the equilibrium wind vectors during nighttime, daytime, the daytime morning hours, and the daytime afternoon hours, respectively. The dashed lines represents the radius of the circular arcs.

Fig. 12: Schematic hodographs of the zonal (u) and meridional winds (v) at (a) 30°S and (b)-(c) 90°S. The red and blue colored arcs indicate the daytime and nighttime hodographs, respectively. N and D denote daytime and nighttime, respectively, for $(u_{\mathrm{eq}}, v_{\mathrm{eq}})$. AM and PM denote morning and evening values of $(u_{\mathrm{eq}}, v_{\mathrm{eq}})$, respectively.

Fig. 13: Amplitude of inertial oscillation as a function of the geostrophic and initial wind components at 30°S and 50°S. The black circles represent the average amplitudes on the third and fourth days, and the black dotted line interpolates these black circles. The red and blue circles represent amplitude for the third and fourth

model days, respectively.

Fig. 14: Vertical profiles of the zonal wind component at 30°S during the nighttime at an interval of 3 h.

Fig. 15: Frequency power spectra in energy-content form for the zonal wind component [$P(\omega)\omega$] that is a function of height at 30°S (bottom left), 50°S (bottom right), 14.47°S (top left) and 90°S (top right). The units of the power spectra are m^2 s^{-2}. Tones are drawn for $10 \log P(\omega)\omega$. The thick black lines indicate each inertial frequency. Three dashed lines indicate frequencies of one day, a half a day and 6 h, respectively.

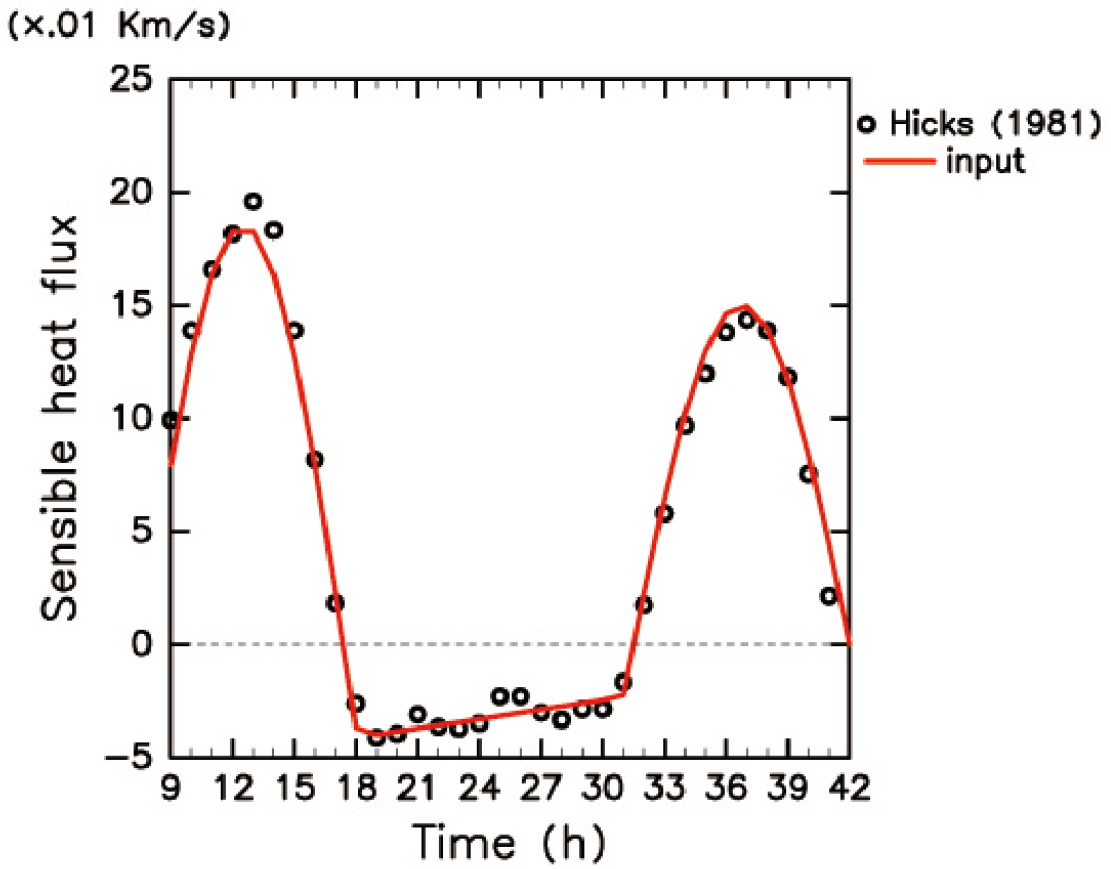

Fig.1: Time series of surface sensible flux (Km s^{-1}) as provided by the model in the Wangara simulation. The dots represent estimates from the observational results (Hicks 1981).

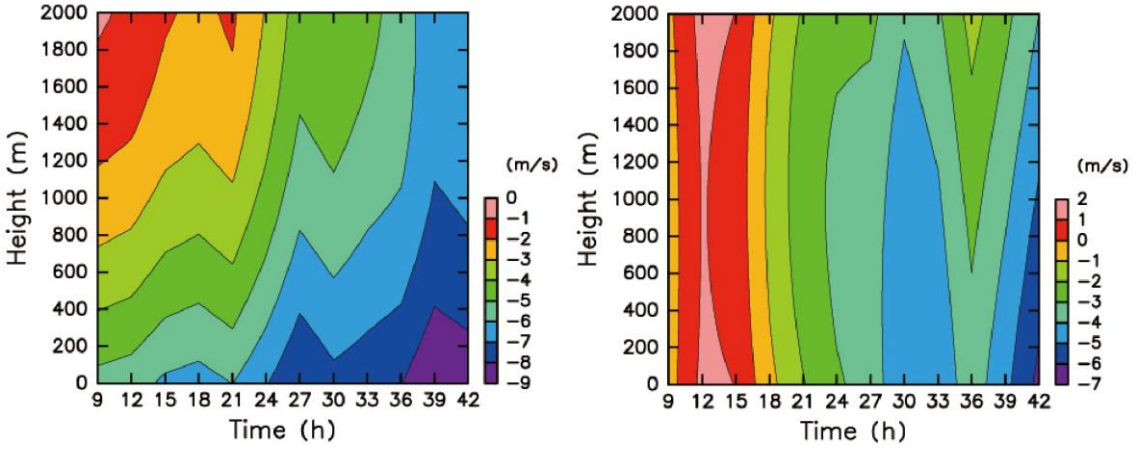

Fig.2: Time-height cross sections of the observed (left) zonal (U_g) and (right) meridional (V_g) components of geostrophic wind (m s^{-1}) (Yamada and Mellor 1975).

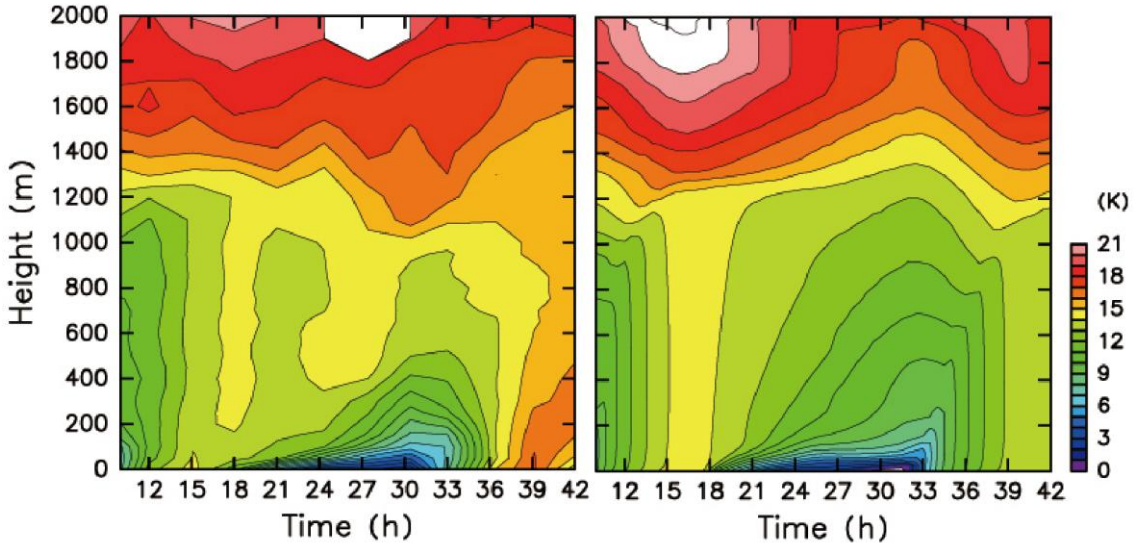

Fig.3: Time-height cross sections of the (left) observed and (right) simulated horizontally-averaged potential temperature (°C).

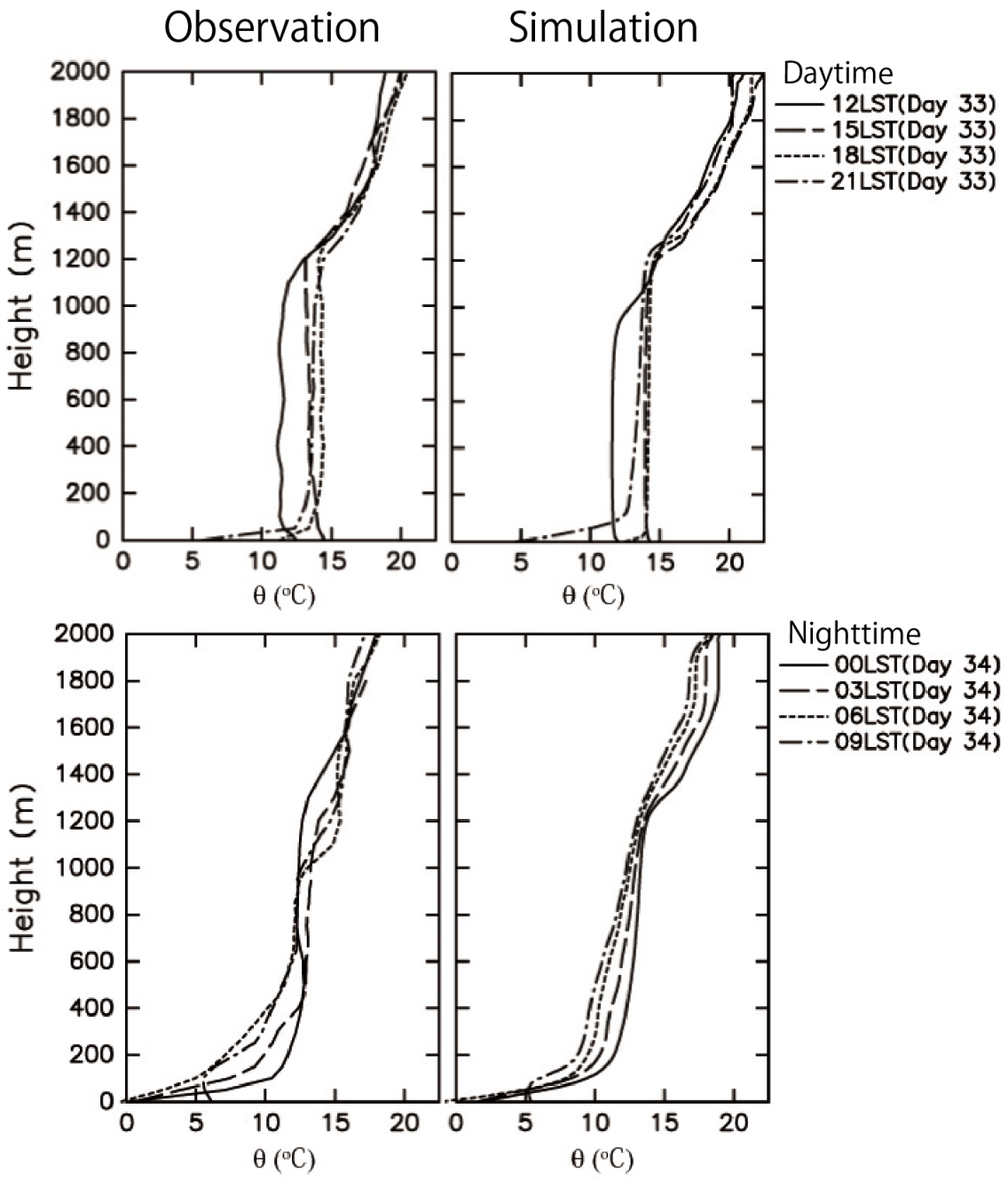

Fig.4: Vertical profiles of (left) observed and (right) simulated daytime (top) and nighttime (bottom) mean potential temperature.

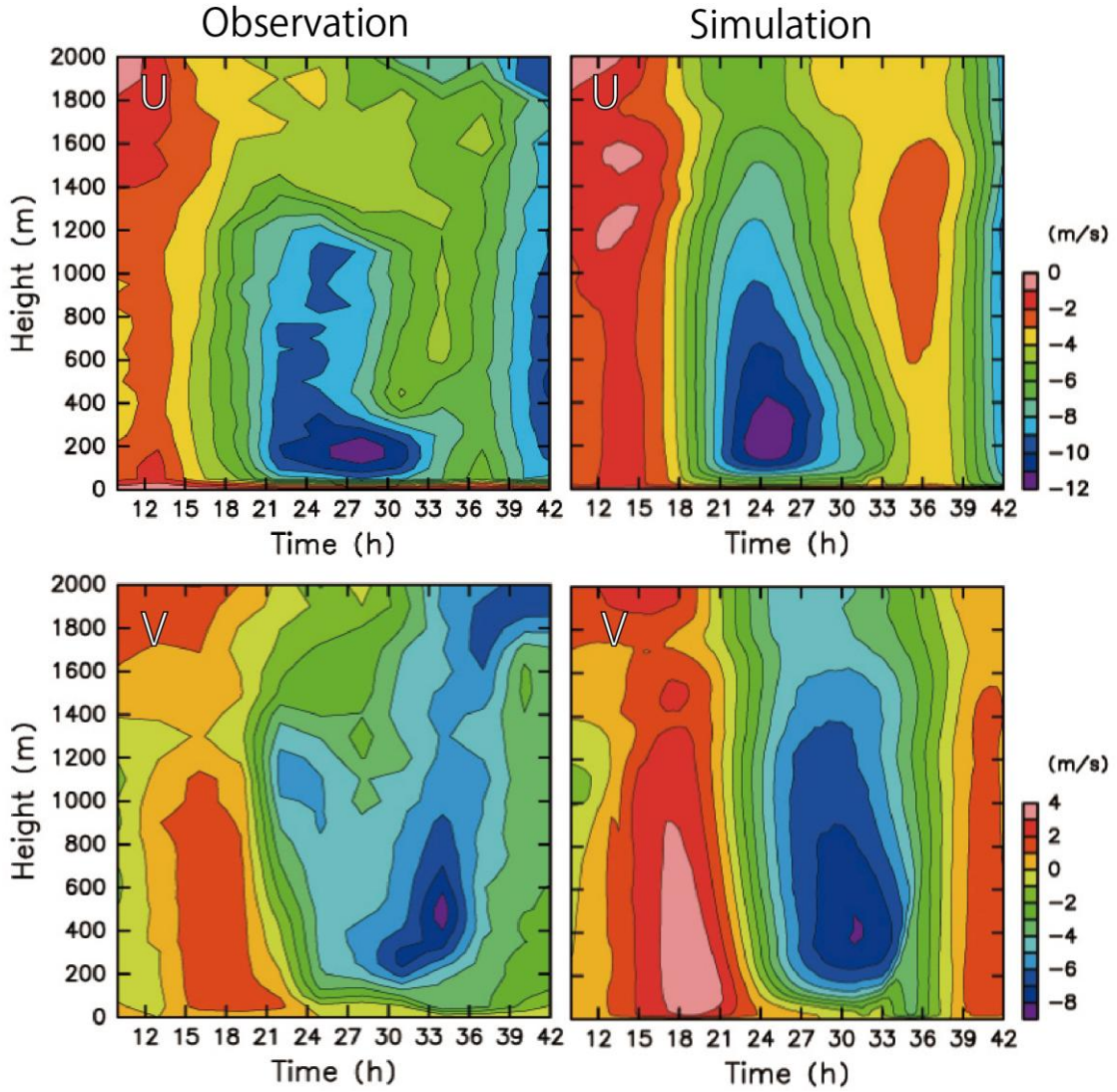

Fig.5: Time-height cross sections of horizontally-averaged (left) observed and (right) simulated (top) zonal and (bottom) meridional wind speed (m s^{-1}).

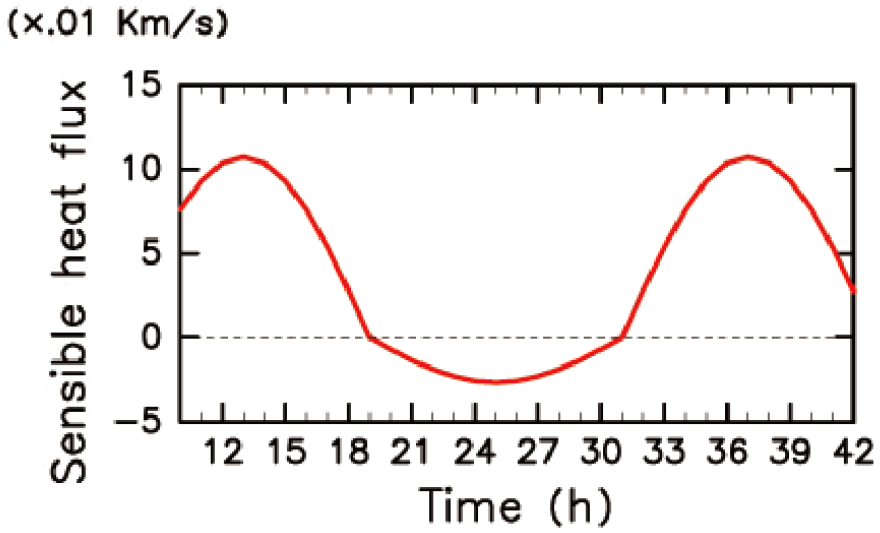

Fig.6: Time series of surface sensible flux (Km s^{-1}) as provided by the model in the diurnal cycle simulation.

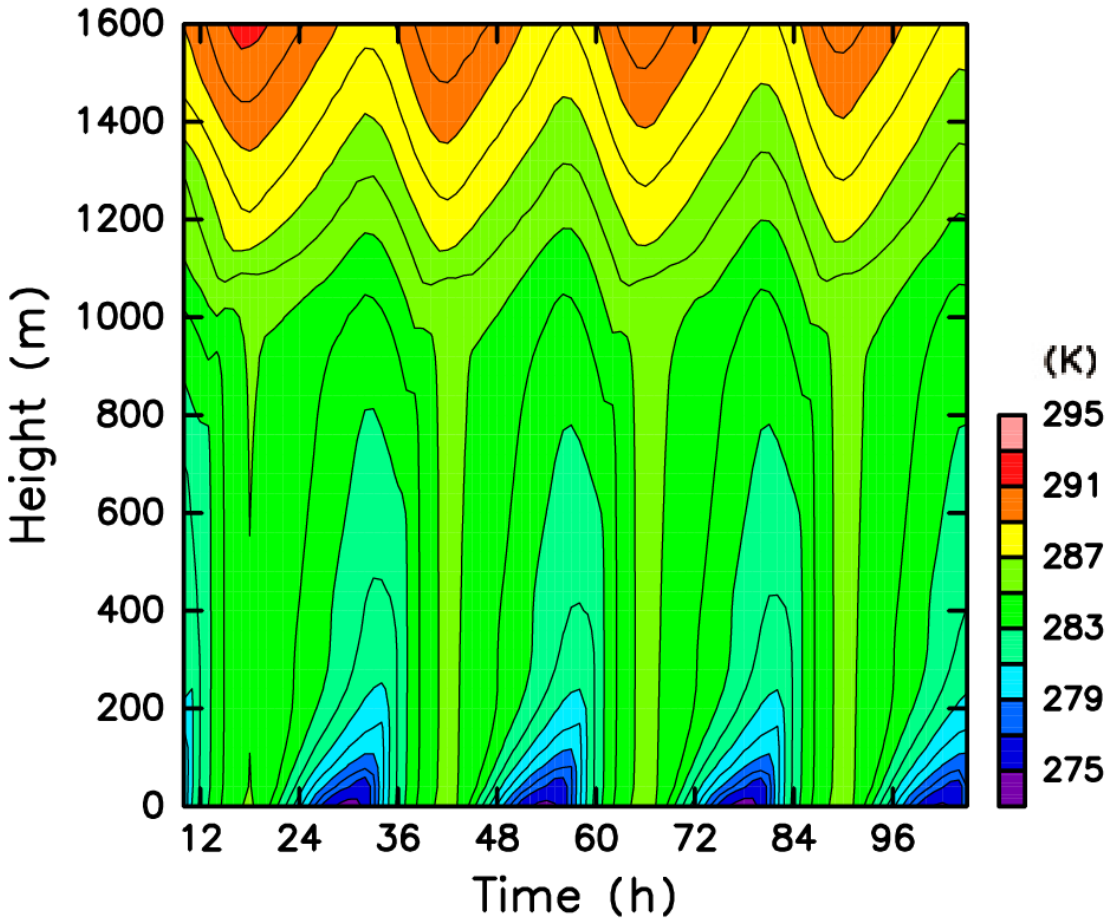

Fig.7: Time-height cross section of horizontally-averaged simulated potential temperature (K) at 50°S.

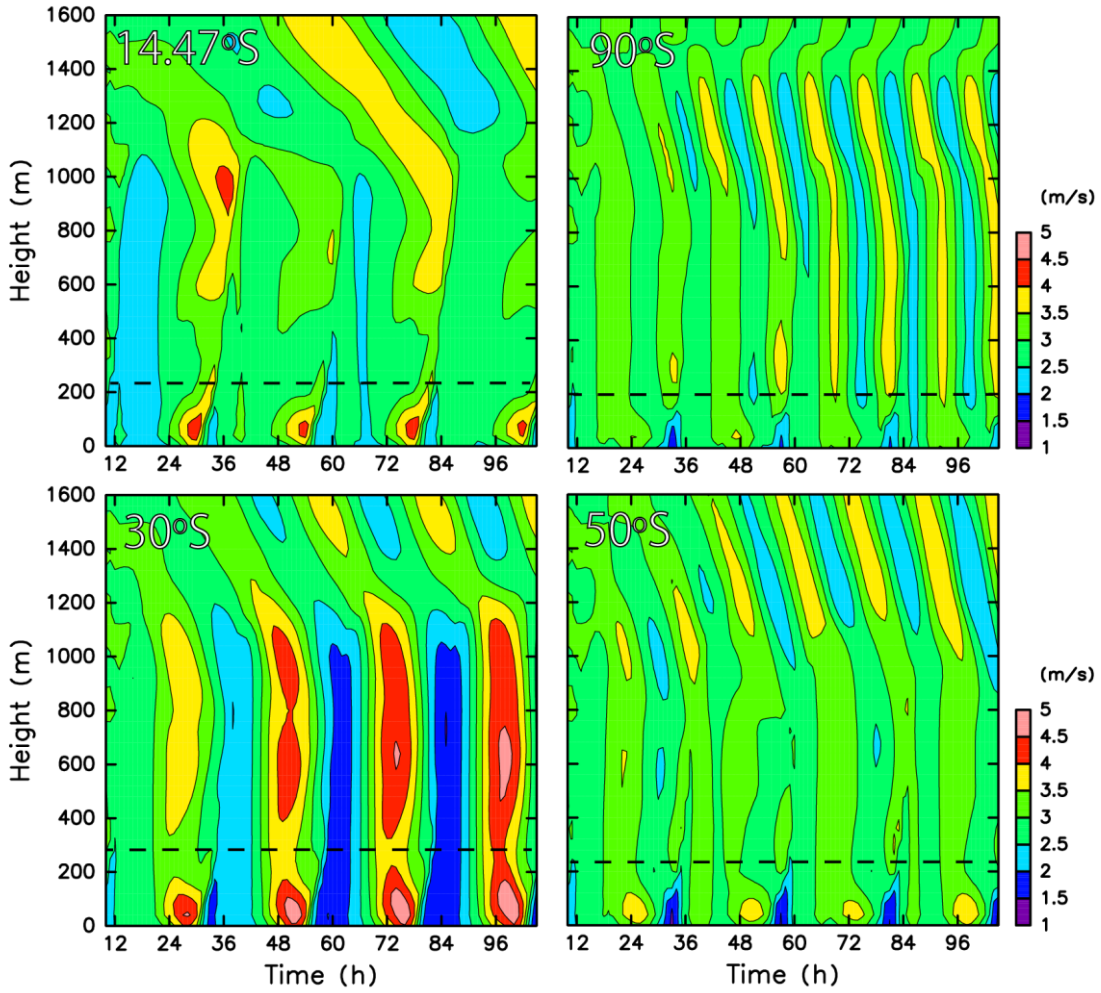

Fig.8: Time-height cross sections of horizontally-averaged simulated zonal wind speed (m s^{-1}) at (left, bottom) 30°S, (right, bottom) 50°S, (left, top) 14.47°S and (right, top) 90°S. The dashed line indicate the maximum height of the nocturnal stable boundary layer.

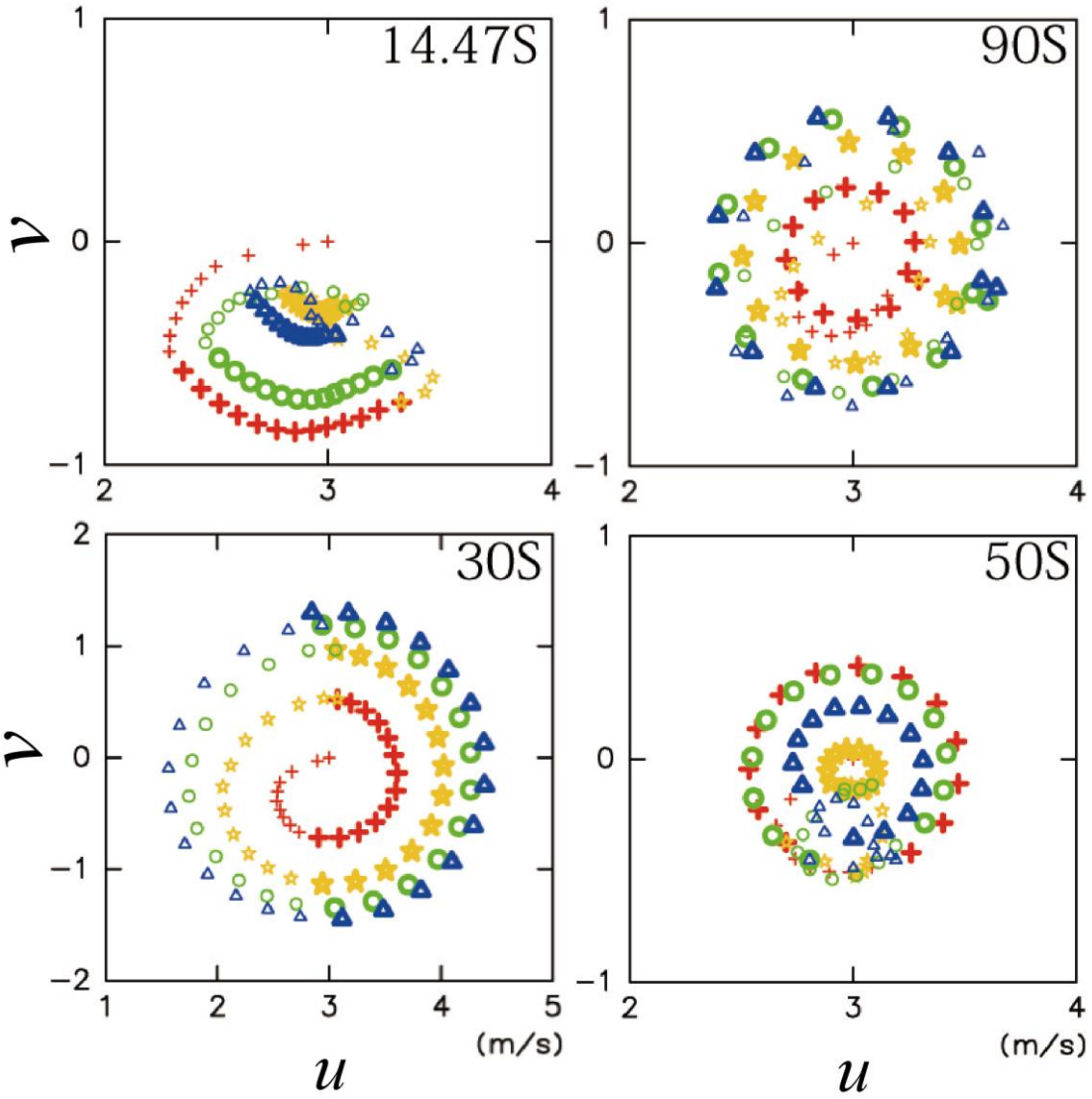

Fig. 9: Simulated hodographs of zonal (u) and meridional winds (v) at 30°S (bottom left), 50°S (bottom right), 90°S (top left), and 14.47°S (top right). The height-averaged of the 200-800m wind is presented. Each mark denotes the values of (u, v) at time intervals of one hour. The thick marks denote nighttime (19:00 LST – 07:00 LST) and the thin marks denote daytime (07:00 LST – 19:00 LST) values. The red, yellow, green and blue colors represent data for the first, second, third, and fourth days from the initiation of integration, respectively.

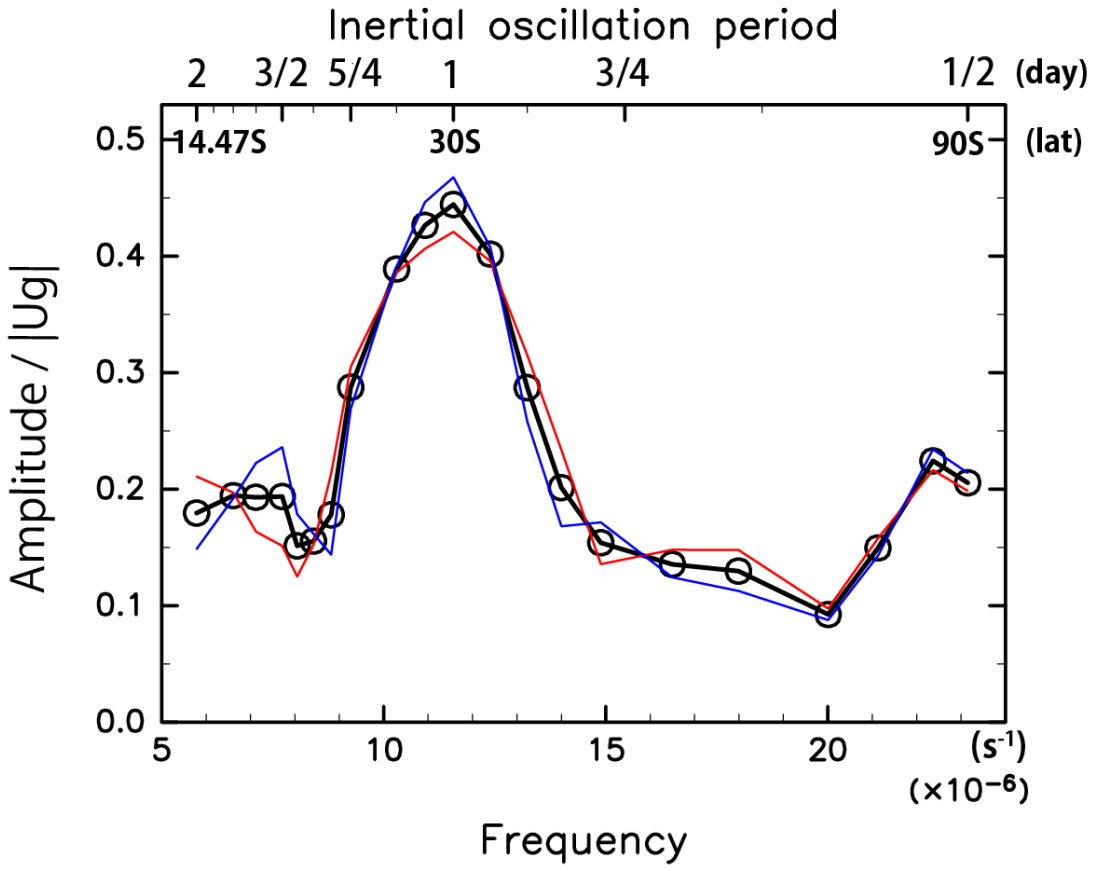

Fig. 10: Oscillation amplitude as a function of latitude for $(u_g, v_g) = (3, 0)$ (m/s). Inertial frequency (bottom), latitude (middle) and an inertial period (top) are shown. The red and blue lines represent the amplitude on the third and fourth model days, respectively. The black thick line represents the average amplitude for the third and fourth days.

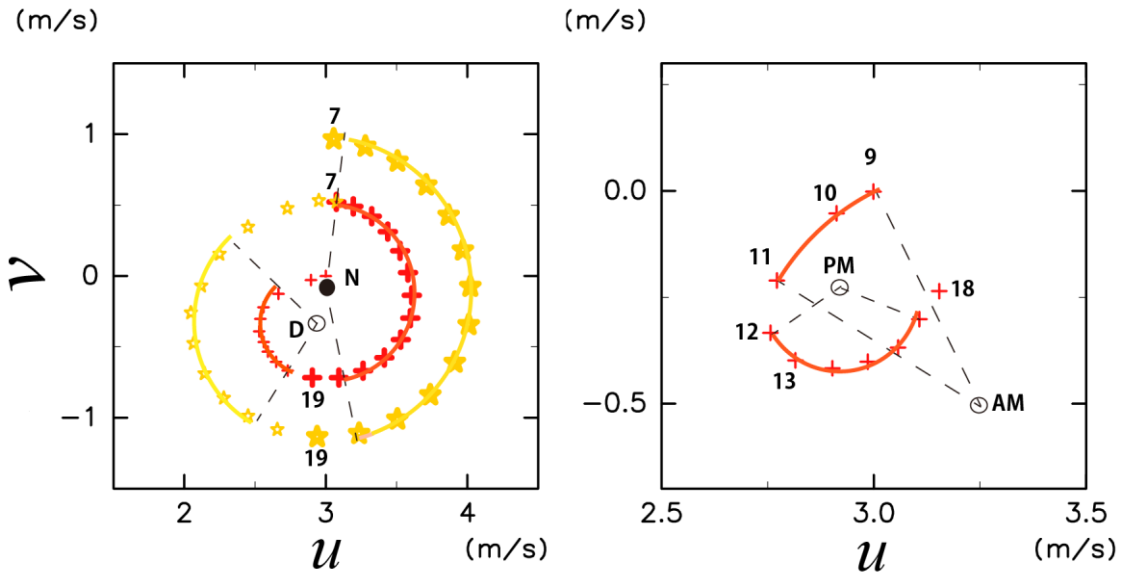

Fig. 11: Simulated hodographs of the zonal (u) and meridional winds (v) at 30°S (left) and 90°S (right). The same marks in Fig. 10 are used. The numerals in the figures denote local time. N, D, AM, and PM denote the equilibrium wind vectors during nighttime, daytime, the daytime morning hours, and the daytime afternoon hours, respectively. The dashed lines represents the radius of the circular arcs.

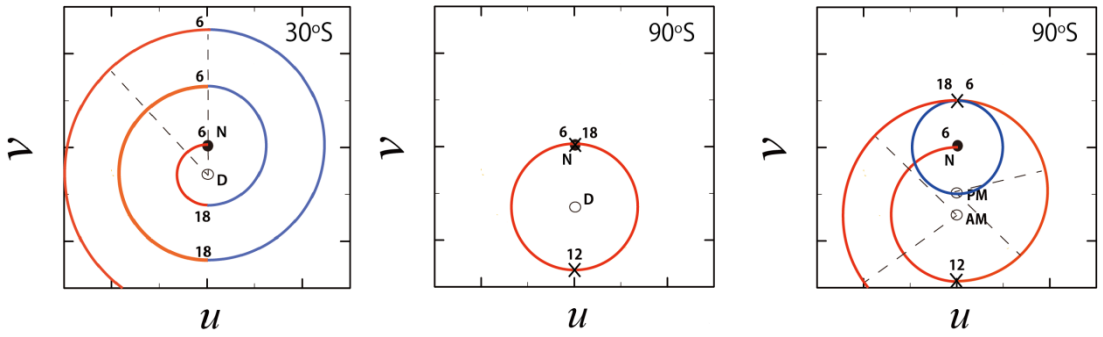

Fig. 12: Schematic hodographs of the zonal (u) and meridional winds (v) at (a) 30°S and (b)-(c) 90°S. The red and blue colored arcs indicate the daytime and nighttime hodographs, respectively. N and D denote daytime and nighttime, respectively, for $(u_{\mathrm{eq}}, v_{\mathrm{eq}})$. AM and PM denote morning and evening values of $(u_{\mathrm{eq}}, v_{\mathrm{eq}})$, respectively.

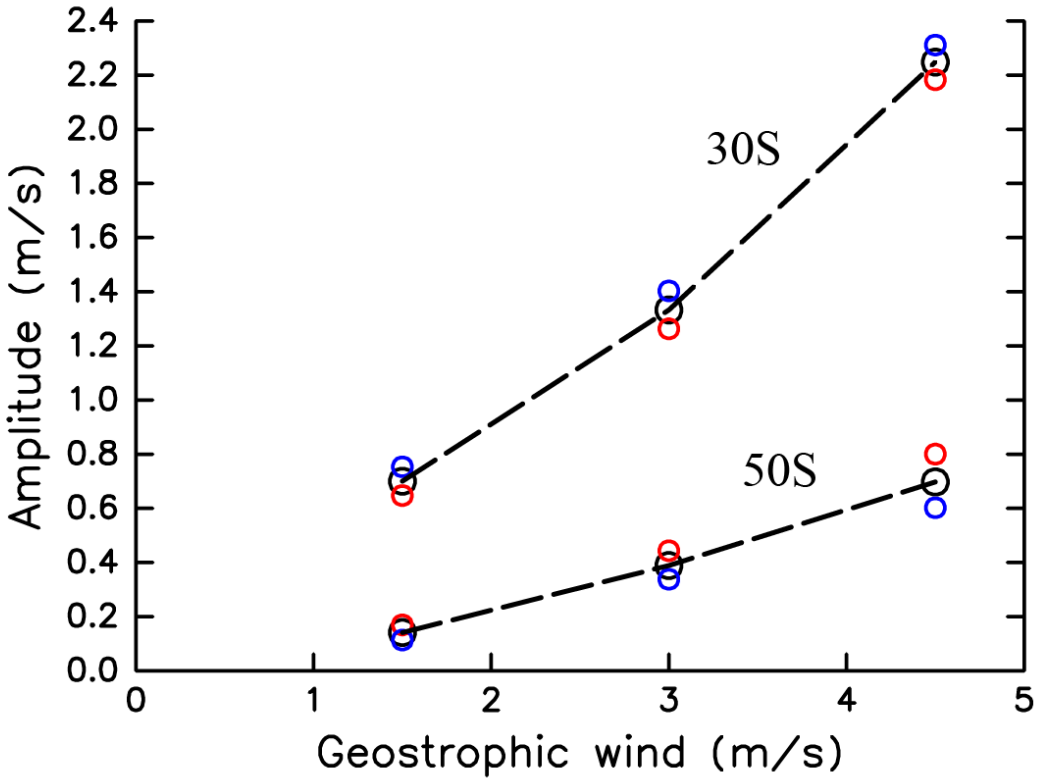

Fig. 13: Amplitude of inertial oscillation as a function of the geostrophic and initial wind components at 30°S and 50°S. The black circles represent the average amplitudes on the third and fourth days, and the black dotted line interpolates these black circles. The red and blue circles represent amplitude for the third and fourth model days, respectively.

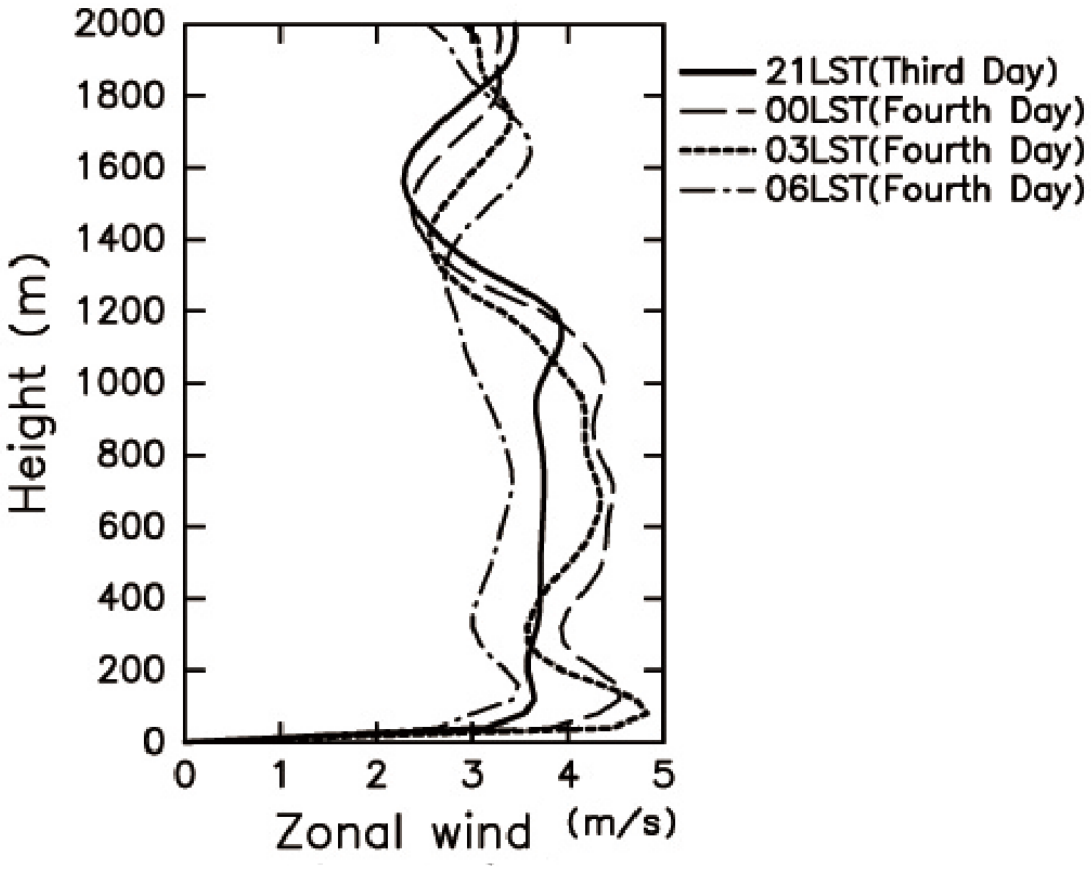

Fig.14: Vertical profiles of the zonal wind component at 30°S during the nighttime at an interval of 3 h.

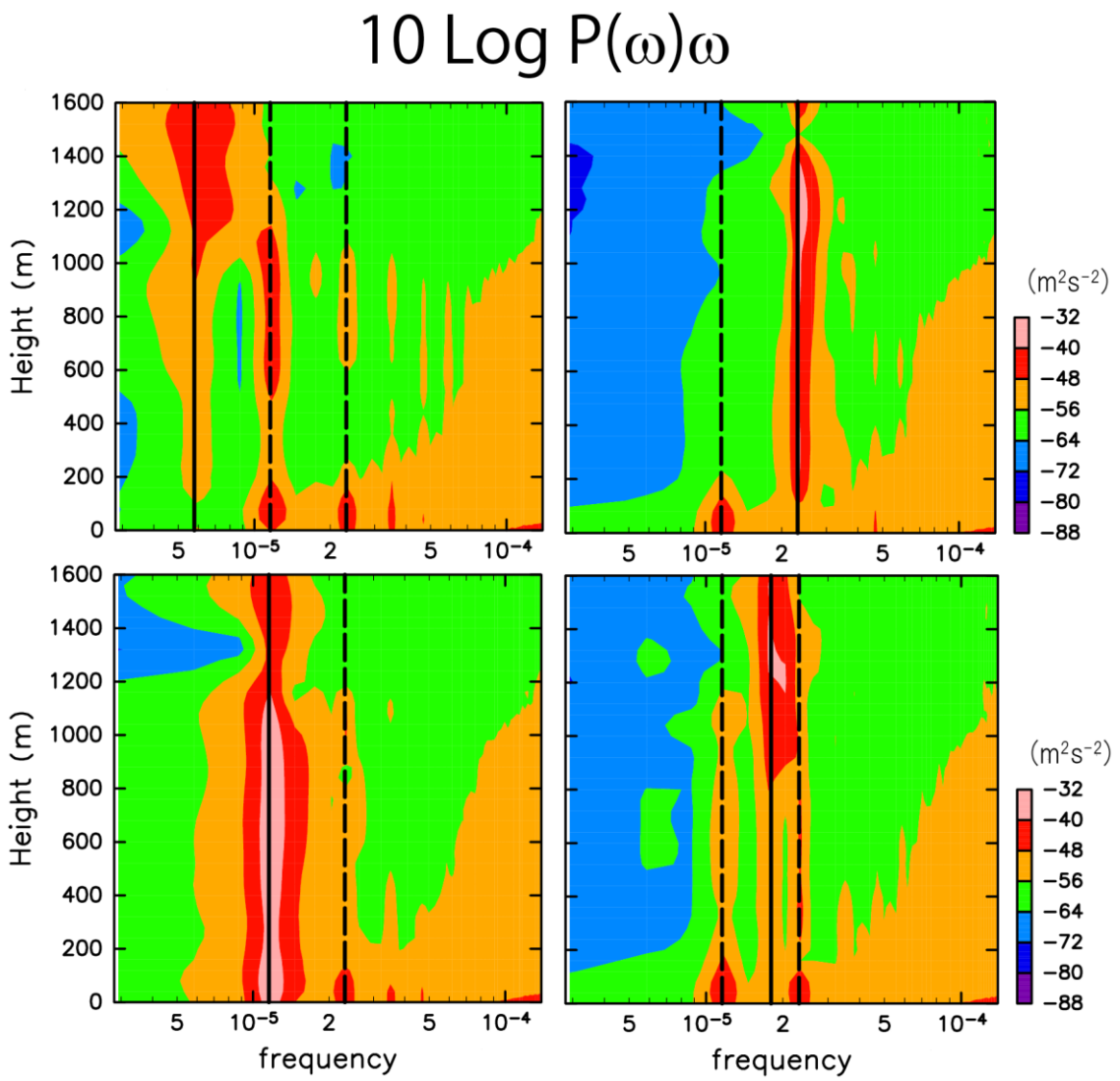

Fig. 15: Frequency power spectra in energy-content form for the zonal wind component [$P(\omega)\omega$] that is a function of height at 30°S (bottom left), 50°S (bottom right), 14.47°S (top left) and 90°S (top right). The units of the power spectra are m^2 s^{-2}. Tones are drawn for $10 \log P(\omega)\omega$. The thick black lines indicate each inertial frequency. Three dashed lines indicate frequencies of one day, a half a day and 6 h, respectively.